

See discussions, stats, and author profiles for this publication at: <https://www.researchgate.net/publication/231171537>

# Cyclic Voltammetric Responses for Inlaid Microdisks with Shields of Thickness Comparable to the Electrode Radius: A Simulation of Reversible Electrode Kinetics

ARTICLE *in* ANALYTICAL CHEMISTRY · APRIL 1995

Impact Factor: 5.64 · DOI: 10.1021/ac00103a018

---

CITATIONS

34

---

READS

18

2 AUTHORS, INCLUDING:



Johna Leddy

University of Iowa

57 PUBLICATIONS 749 CITATIONS

SEE PROFILE

# Cyclic Voltammetric Responses for Inlaid Microdisks with Shields of Thickness Comparable to the Electrode Radius: A Simulation of Reversible Electrode Kinetics

Yun Fang<sup>†</sup> and Johna Leddy<sup>\*‡</sup>

Department of Chemistry and Biochemistry, Queens College and the Graduate Program of the City University of New York, 65-30 Kissena Boulevard, Flushing, New York 11367

Given common methods of preparing inlaid microdisk electrodes, shield thicknesses are often comparable to disk radii. Equations appropriate to characterizing the steady state, cyclic voltammetric response for microdisks embedded in infinite insulating planes poorly approximate the steady state response at these electrodes because, on the time scale to achieve steady state, diffusion around the shield from behind the plane of the electrode contributes to the flux. A finite difference simulation with a nonuniform, expanding spatial grid is presented for reversible electrode kinetics over a range of scan rates sufficient to follow the transition from linear to radial diffusion, including flux around the edge of the shield. The voltammetric response is influenced critically by shield thickness and electrode radius; a method is proposed and verified experimentally to determine radius and shield thickness. The equations for infinitely thick insulators underestimate the current at a thinly shielded microdisk by  $\leq 49\%$ . Generation of a nonuniform, expanding grid is presented.

Microelectrodes have become a major tool for studying nonstandard electrochemical systems. Solutions without added electrolyte,<sup>1-5</sup> frozen solutions,<sup>6</sup> and gas phase environments<sup>7-12</sup>

are examples of matrices that the use of microelectrodes has opened to inspection by electrochemical methods. Drawing on knowledge of polarographic responses, electrochemists have interpreted the voltammetric responses of microelectrodes using the current response expected for spherical and hemispherical electrodes. For hemispherical microelectrodes, this is appropriate. For disks inlaid in semiinfinite insulators, Oldham and Zoski<sup>13</sup> have shown the steady state currents at the disk and the hemisphere are the same within a multiplication constant ( $4/\pi$ ) when the radii of the hemisphere and disk are equal. For inlaid disks where the insulating shield is not large compared to either the electrode radius or the diffusion length generated during the course of the sweep, this approximation has limitations and will underestimate the steady state current because of diffusion from behind the plane of the electrode.

Microelectrodes have been constructed as inlaid disks with radii as small as 1 nm,<sup>14</sup> but diameters are typically 100 nm to 100  $\mu\text{m}$ . Two common methods of electrode construction are either to draw down a capillary around a wire<sup>15</sup> or to dip coat an insulating polymer on the outer surface of a cylindrical conductor such as a carbon fiber.<sup>16</sup> With these construction methods, the thickness of the insulating shield and the radius of the disk are comparable, and on the time scale of standard voltammetric perturbations, the diffusion field undergoes a transition from linear to radial symmetry and is established radially behind the plane of the electrode and shield. How much the flux from behind the plane of the electrode enhances the current will depend on the size of the electrode and the shield. Consider the typical glass capillary, carbon fiber microelectrode, with a disk radius of about 3  $\mu\text{m}$ , concentric shield thickness of about 7  $\mu\text{m}$ , and microdisk assembly diameter of 20  $\mu\text{m}$ . For a cyclic voltammetric sweep at 0.1 V/s over 1 V, the diffusion length and a surface concentration significantly different from the bulk concentration will be established for roughly 10 s. If the voltammetric response is to be interpreted using the steady state response for a hemispherical electrode, two conditions must be met. First, the system must be at steady state. Steady state is established once the diffusion length,  $l \equiv (2Dt)^{1/2}$ , is large compared to the disk radius,  $r_0$ . For

<sup>†</sup> Present address: American Cyanamid, Princeton, NJ.

<sup>‡</sup> Present address: Department of Chemistry, The University of Iowa, Iowa City, IA 52242.

- (1) Dibble, T.; Bandyopadhyay, S.; Ghoroghchian, J.; Smith, J. J.; Sarfarazi, F.; Fleischmann, M.; Pons, S. *J. Phys. Chem.* **1986**, *90*, 5275-5277.
- (2) Cassidy, J.; Khoo, S. B.; Pons, S.; Fleischmann, M. *J. Phys. Chem.* **1985**, *89*, 3933-3935.
- (3) Bond, A. M.; Lay, P. A. *J. Electroanal. Chem.* **1986**, *199*, 285-295.
- (4) Bond, A. M.; Fleischmann, M.; Robinson, J. *J. Electroanal. Chem.* **1984**, *168*, 299-312.
- (5) Howell, J. O.; Wightman, R. M. *Anal. Chem.* **1984**, *56*, 524-529.
- (6) Bond, A. M.; Fleischmann, M.; Robinson, J. *J. Electroanal. Chem.* **1984**, *180*, 257-263.
- (7) Ghoroghchian, J.; Sarfarazi, F.; Dibble, T.; Cassidy, J.; Smith, J. J.; Russell, A.; Dunmore, G.; Fleischmann, M.; Pons, S. *Anal. Chem.* **1986**, *58*, 2278-2282.
- (8) Brina, R.; Pons, S.; Fleischmann, M. *J. Electroanal. Chem.* **1988**, *244*, 81-90.
- (9) Brina, R.; Pons, S. *J. Electroanal. Chem.* **1989**, *264*, 121-130.
- (10) Jernigan, J. C.; Chidsey, C. E. D.; Murray, R. W. *J. Am. Chem. Soc.* **1985**, *107*, 2824-2826.
- (11) Geng, L.; Redd, R. A.; Kim, M.-H.; Wooster, T. T.; Oliver, B. N.; Egekeze, J.; Kennedy, R. T.; Jorgenson, J. W.; Parcher, J. F.; Murray, R. W. *J. Am. Chem. Soc.* **1989**, *111*, 1614-1619.
- (12) Parcher, J. F.; Barbour, C. J.; Murray, R. W. *Anal. Chem.* **1989**, *61*, 584-589.

(13) Oldham, K. B.; Zoski, C. G. *J. Electroanal. Chem.* **1988**, *256*, 11-19.

(14) Penner, R. M.; Heben, M. J.; Longin, T. L.; Lewis, N. S. *Science* **1990**, *250*, 1118-1121.

(15) Dayton, M. A.; Brown, J. C.; Stutts, K. J.; Wightman, R. M. *Anal. Chem.* **1980**, *52*, 946.

(16) Potje-Kamloth, K.; Janata, J.; Josowicz, M. *Ber. Bunsen-Ges. J. Phys. Chem.* **1989**, *93*, 1480-1485.

time,  $t = 10$  s, and diffusion coefficient,  $D = 5 \times 10^{-6}$  cm<sup>2</sup>/s,  $l = 100$   $\mu$ m. Then,  $l/r_0 \approx 33$ ; the system is at steady state. Second, diffusion from around the edges of the insulating shield from behind the plane of the electrode must be avoided. Given  $l = 100$   $\mu$ m and a 7  $\mu$ m thick shield, diffusion around the edges will definitely occur. If the scan rate is increased sufficiently that diffusion from behind the plane of the shield is precluded, then  $l \leq 7$   $\mu$ m and the system will no longer be at steady state because  $l/r_0 \leq 2.3$ . Diffusion from behind the plane of the electrode will enhance currents.

Shoup and Szabo were the first to recognize that diffusion from behind the plane of the electrode enhances flux to an electrode.<sup>17,18</sup> They simulated the chronoamperometric current response for finitely shielded electrodes using a hopscotch algorithm and spatial and temporal grids of fixed size.<sup>17,18</sup> They found the steady state current increased as shield thickness decreased for a given electrode radius. Because steady state current is independent of the voltage perturbation used to achieve steady state, the steady state cyclic voltammetric currents should increase similarly. Shoup and Szabo stated simulations of electrodes with finite shields are difficult because of the discontinuous derivatives in concentration about the insulator/solution interface in the plane of the electrode. Essentially, concentration gradients change rapidly about this interface, and it is critical that these changes be modeled well if an accurate current is to be simulated. In a fixed grid simulation, the number of grid elements needed to simulate this interface well is so large that the computational time is prohibitive.

Shoup and Szabo introduced hopscotch finite difference methods for electrochemical simulations,<sup>17,18</sup> and Feldberg<sup>19</sup> identified conditions where care must be exercised to use hopscotch methods reliably. Several sophisticated methods have been introduced in the interim. Implicit DuFort Frankel methods are robust and efficient.<sup>20,21</sup> Conformal mapping has been coupled to simulation to model microdisks in infinite insulating planes.<sup>23,24</sup> Expanding spatial grids have proven a powerful tool for diffusion simulations<sup>19–22</sup> because of improved resolution near interfaces and edges. In this paper, expanding grids are used in an explicit finite difference simulation. For reaction schemes more complex than reversible electron transfer, a more efficient (although not more accurate) simulation could be performed by coupling hopscotch or DuFort Frankel methods with the grid defined below.

Here, we present a computer simulation for the effect of shield thickness on the cyclic voltammetric response of an inlaid microdisk, over a scan rate range sufficient to follow the transition from linear to steady state diffusion. The simulation is restricted to reversible electrode kinetics and a switching potential 250 mV past the formal potential. The simulation is a two-dimensional, finite difference simulation in cylindrical coordinates. Expanding spatial grids<sup>19–22</sup> are employed in both the axial and radial

coordinates, where the axial expansion is uniform and the radial expansion is not. Because there are two pivotal interfaces in the radial coordinate, the electrode/insulator and insulator/solution interfaces, more refined grids are needed at these two junctures. The radial grid expands from the edge of the electrode/insulator interface to the midpoint of the insulator where it begins to contract again as the insulator/solution interface is approached. The radial grid then expands again as distance from the insulator edge is increased. The method for defining this nonuniform grid is presented. Methods for verifying the accuracy of the simulation are outlined in detail, and algorithms for characterizing steady state and the approach to steady state under cyclic voltammetric conditions are presented. Several questions about the response of electrodes with finite shields are addressed: (1) How does the thickness of the insulating shield influence the voltammetric response? (2) How is steady state recognized at a disk inlaid in a thin shield, and how is convergence to steady state affected by diffusion from behind the plane of the electrode? (3) How are disk radius and shield thickness determined from cyclic voltammograms? (4) What are the limitations of using equations appropriate to infinitely thick insulating shields to interpret the voltammetric response of inlaid disk electrodes with thin shields?

## EXPERIMENTAL SECTION

Experimental studies were performed to verify the correctness of the cyclic voltammetric method proposed to determine the electrode radius and shield thickness.

**Electroactive Species and Solvents.** Potassium ferricyanide (Baker Chemicals) and dopamine (3-hydroxytyramine) hydrochloride (Aldrich Chemicals) were used as redox species, and sodium sulfate (anhydrous, reagent ACS, MCB Manufacturing Chemicals, Inc.) and hydrochloric acid were the respective electrolytes. Solution concentrations were 2.0 mM for the redox species and 0.1 M for the electrolytes. Distilled water was purified through a Milli-Q, QM-140 (Millipore Corp.). Test solution were degassed with water presaturated nitrogen for 0.5 h before the measurements were made.

**Electrodes.** Working electrodes were made by drawing a glass capillary down around a carbon fiber.<sup>15</sup> A carbon fiber (6–8  $\mu$ m in diameter) was inserted into a 5  $\mu$ L micropipet (Becton Dickinson Co.). Vacuum was pulled on one end of the pipet, while the midsection of the pipet was heated in a bunsen burner flame. As the glass constricted, the fiber became well sealed in the softened glass. The vacuum enhanced the constriction of the glass around the carbon fiber. By cutting through the constriction, perpendicular to the carbon fiber, two carbon microdisks with glass sheaths were formed. Inside the glass tube, connection was made to the carbon fiber with silver epoxy (AESAR, Johnson Matthey Co.) and a fine copper wire. The top was sealed with epoxy to provide mechanical stability. The resulting electrode assemblies were about 1 cm long. The radius of the carbon fiber was determined by scanning electron microscopy (SEM; Hitachi S-570). The thickness of the glass insulator varies from electrode to electrode and was also measured by SEM. Silver wire was used as a quasi-reference electrode and a 4 cm<sup>2</sup> platinum screen was used as the counter electrode.

**Instruments and Measurement.** Cyclic voltammetry was performed with a Princeton Applied Research Model 173 potentiostat and Model 175 universal programmer, and results were recorded on a Norland 300 processing digital oscilloscope and an  $x$ - $y$  recorder (Soltec). Resistance was compensation by

(17) Shoup, D.; Szabo, A. J. *Electroanal. Chem.* **1982**, *140*, 237–245.

(18) Shoup, D.; Szabo, A. J. *Electroanal. Chem.* **1984**, *160*, 27–31.

(19) Feldberg, S. W. J. *Electroanal. Chem.* **1987**, *222*, 101–106.

(20) Feldberg, S. W. J. *Electroanal. Chem.* **1990**, *290*, 49–65.

(21) Lerke, S. A.; Evans, D. H.; Feldberg, S. W. J. *Electroanal. Chem.* **1990**, *296*, 299–315.

(22) Feldberg, S. W. J. *Electroanal. Chem.* **1981**, *127*, 1–10.

(23) Amatore, C. A.; Deakin, M. R.; Wightman, R. M. J. *Electroanal. Chem.* **1986**, *206*, 23–26.

(24) Micheal, A. C.; Wightman, R. M.; Amatore, C. A. J. *Electroanal. Chem.* **1989**, *263*, 33–45.

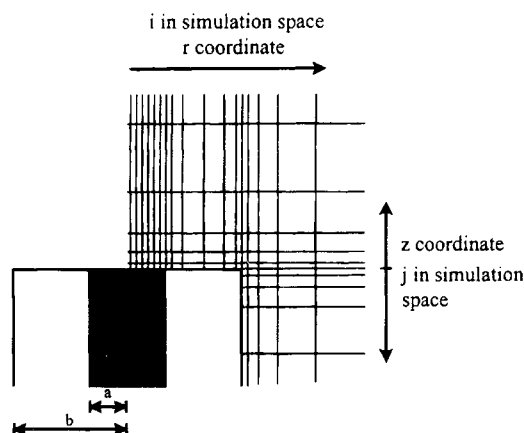


**Figure 1.** Schematic of the electrode geometry. The active electrode surface is pointed to the top of the page; the longitudinal cross section is shown. The real and simulation coordinates are illustrated. The electrode radius is  $a$ , while the radius of the electrode and insulator is  $b$ . The radial coordinate,  $r$ , is expressed as  $i$  in the simulation, while the longitudinal coordinate,  $z$ , is expressed as  $j$ .  $i = 0$  at the center of the electrode.  $j < 0$  and  $j > 0$ , respectively, below and above the plane of the electrode surface. The finer resolution of the grid is seen across the electrode surface, at the electrode/insulator and insulator/solution interfaces. The resolution is needed here to accurately map the transitions to radial diffusion that occurs at these edges.

positive feedback. All measurements were carried out in a Faraday cage at room temperature, and 5 min was allowed between measurements to ensure the system had reequilibrated. Data were collected for each electrode at several different scan rates.

## PARAMETERIZATION AND SIMULATION

**Electrochemical Reaction Model.** The model is developed for a reversible heterogeneous electron transfer reaction at an inlaid microdisk:



In Figure 1, the longitudinal cross section of the microelectrode assembly is shown, where the active electrode surface is pointed to the top of the page. The disk, of radius,  $a$ , is encircled by the insulator. The radius of the entire electrode assembly, including the disk and insulator, is  $b$ .

The electrode is modeled by the transport equation expressed in cylindrical coordinates. As the system is axially symmetric, no angular coordinate is needed.

$$\frac{\partial c(z,r,t)}{\partial t} = D \left[ \frac{\partial^2 c(z,r,t)}{\partial r^2} + \frac{1}{r} \frac{\partial c(z,r,t)}{\partial r} + \frac{\partial^2 c(z,r,t)}{\partial z^2} \right] \quad (2)$$

$r$  is the radial coordinate, parallel to the plane of the electrode surface;  $z$  is the coordinate perpendicular to the electrode surface.  $r = 0$  at the center of the disk.  $z = 0$  at the surface of the electrode, positive above and negative below the plane of the electrode.  $t$ ,  $D$ , and  $c(z,r,t)$  are time, diffusion coefficient, and space- and time-dependent concentrations, respectively.

Based on Faraday's equation and Fick's first law, the time-dependent current,  $i(t)$ , is set by the total flux normal to

the electrode surface at  $t$ ,

$$\frac{i(t)}{nFA} = D \int_0^{2\pi a^2} \left[ \frac{\partial c(z,r,t)}{\partial z} \right]_{z=0} dA = 2\pi D \int_0^a r \left[ \frac{\partial c(z,r,t)}{\partial z} \right]_{z=0} dr \quad (3)$$

where  $n$ ,  $F$ , and  $A$  are the number of electrons transferred, Faraday's constant, and the electrode area, respectively.

The diffusion coefficients of the oxidized and reduced species are taken as equal, which leads to  $c_A(z,r,t) + c_B(z,r,t) = c_A^\circ$ .  $c_A^\circ$  is the bulk and initial concentration. Given these constraints, the problem is completely specified by  $c_A(z,r,t)$  alone. For reversible electron transfer kinetics,

$$\exp[nF(E^\circ - E)/RT] = \frac{c_B(0,r,t)}{c_A(0,r,t)} = \frac{c_A^\circ - c_A(0,r,t)}{c_A(0,r,t)} \quad (4)$$

where  $0 \leq r < a$ , and  $E^\circ$  is the formal potential.  $F/RT = 38.92 \text{ V}^{-1}$ ;  $T = 298.0 \text{ K}$ .  $R$  is the gas constant.

For linear sweep cyclic voltammetry, the initial potential is  $E_o$  and the switching potential is  $E_f$ . All potentials are in units of volts. For a scan rate,  $v$  (V/s), the total time for the sweep is  $T_t = 2[E_f - E_o]/v$ . For potential,  $E(t)$

$$E(t) = \begin{cases} E_o - vt & 0 \leq t \leq T_t/2 \\ E_o - v(T_t - t) & T_t/2 < t \leq T_t \end{cases} \quad (5)$$

The boundary and initial conditions for eq 2 are as follows. For the initial condition,

$$\begin{cases} r \geq 0, z \geq 0, t = 0 \\ r > b, z < 0, t = 0 \end{cases} \quad c_A(z,r,t) = c_A^\circ \quad (6)$$

All of the following are boundary conditions, applicable for  $t > 0$ .

$$0 \leq r < a, z = 0 \quad \text{flux}_A(r) = -D_A \left[ \frac{\partial c_A(z,r,t)}{\partial z} \right]_{z=0} \quad (7)$$

$$0 \leq r < a, z = 0 \quad c_A(0,r,t) = \frac{c_A^\circ}{1 + \exp[nF(E^\circ - E)/RT]} \quad (8)$$

$$b > r > a, z = 0 \quad D_A \left[ \frac{\partial c_A(z,r,t)}{\partial z} \right]_{z=0} = 0 \quad (9)$$

$$r \rightarrow \infty, \text{ all } z \quad c_A(z,r,t) = c_A^\circ \quad (10)$$

$$z \rightarrow \infty, \text{ all } r \quad c_A(z,r,t) = c_A^\circ \quad (11)$$

$$r > b, z \rightarrow -\infty \quad c_A(z,r,t) = c_A^\circ \quad (12)$$

$$z \geq 0, r = 0 \quad D_A \left[ \frac{\partial c_A(z,r,t)}{\partial r} \right]_{r=0} = 0 \quad (13)$$

$$z < 0, r = b \quad D_A \left[ \frac{\partial c_A(z,r,t)}{\partial r} \right]_{r=b} = 0 \quad (14)$$

$\text{Flux}_A(r)$  is the flux of species A normal to the electrode surface at radial position  $r$  and  $z = 0$ . Note, eq 8 follows from eq 4. Equations 9 and 14 reflect the impermeability of the insulator to solution species. Equation 13 arises because the system is axially symmetric.

**Table 1. Definition of Grid Distances and Element Sizes for the Nonuniform EESG**

spatial limits	grid limits	grid element width	grid distance <sup>a</sup>
$-\infty < z < \infty$	$-\infty < j < \infty$	$\Delta z_j = \Delta z \exp[\beta( j  - 1)]$	$z_j = \Delta z \frac{\exp[\beta( j  - 0.5)] - 1}{\exp[\beta] - 1}$
$0 < r \leq a^b$	$0 < i \leq N_{ra}$	$\Delta r_i = \Delta r$	$r_i = \Delta r(i - 0.5)$
$a < r < (b - a)/2$	$N_{ra} < i \leq m + N_{ra}^c$	$\Delta r_i = \Delta r \exp[\beta(i - N_{ra} - 1)]$	$r_i = \Delta r \left[ \frac{\exp[\beta(i - N_{ra} - 0.5)] - 1}{\exp[\beta] - 1} + N_{ra} \right]$
$(b - a)/2 < r \leq b$	$m + N_{ra} < i \leq N_{rb}^b$	$\Delta r_i = \Delta r \exp[\beta(N_{rb} - i)]$	$r_i = -\Delta r \left[ \frac{\exp[\beta(i - N_{ra} - 0.5)] - 1}{\exp[\beta] - 1} \right] + \sum_{i=1}^{N_{rb}} \Delta r_i$
$b < r < \infty$	$N_{rb} < i < \infty$	$\Delta r_i = \Delta r \exp[\beta(i - N_{rb} - 1)]$	$r_i = \Delta r \left[ \frac{\exp[\beta(i - N_{rb} - 0.5)] - 1}{\exp[\beta] - 1} \right] + \sum_{i=1}^{N_{rb}} \Delta r_i$

<sup>a</sup> The point in a grid element where the concentration is determined, measured; in the  $z$  coordinate, from the plane of the electrode and, in the  $r$  coordinate, from the center of the disk. <sup>b</sup>  $\Delta r = \Delta z$ ;  $a = N_{ra}\Delta r$ , where  $N_{ra}$  is the number of grid elements across the electrode. <sup>c</sup>  $M$  is the midpoint of the insulator where the grid expands to from the edge of the disk, and where the grid begins to contract again, as the insulator/solution interface is approached.  $M = (N_{rb} - N_{ra})/2$ . <sup>d</sup>  $N_{rb}$  is the number of grid elements across the surface of the electrode and insulator.

**Simulation Model.** The chronoamperometric response of microdisk electrodes has been simulated by Shoup and Szabo<sup>17,18</sup> using a hopscotch algorithm and fixed temporal and spatial grids. The simulation presented here for cyclic voltammetry is carried out by standard explicit finite difference methods, with a fixed time grid and exponentially expanding spatial grids (EESG).<sup>19–22</sup> EESGs offer both significantly more rapid computations and better resolution of concentration profiles at the interfaces between the electrode/insulator and the insulator/solution where small grid elements are used. Grid resolution becomes increasingly coarse as the distance from the electrode surface and interfaces increases. The grid distribution on the electrode surface is shown in Figure 1. Note, the high density of small grid elements across the face of the electrode, at the electrode/insulator interface and around the corner at the insulator/solution interface. The use of small elements in regions where the concentration gradients are steepest results in more accurate descriptions of the flux and, thus, the current response.

The grid in the  $z$  coordinate is expanded uniformly about the plane of the electrode. In EESG, such a uniform expansion is modeled<sup>19,22</sup> as

$$\Delta z_j = \Delta z \exp[\beta(|j| - 1)] \quad (15)$$

where  $\beta$  is the coefficient that sets the rate of spatial expansion.  $\Delta z$  is the size of the smallest grid element in the  $z$  coordinate, and  $j$  numbers the grid elements in the  $z$  coordinate.  $j < 0$  and  $j > 0$  below and above the plane of the electrode, respectively.  $\Delta z_j$  is the thickness of the  $j$ th grid element.  $z_j$  is the distance from the plane of the electrode surface to the point in the  $j$ th element where the concentration is measured.

$$z_j = \frac{\exp[\beta|j| - 0.5] - 1}{\exp[\beta] - 1} \quad (16)$$

As shown in Figure 1, the grid in the radial direction is dense across the electrode surface, expands across the insulator to its midpoint, and then contracts toward the edge of the shield. The radial grid then expands again as the distance from the edge of the shield increases. This expansion is more complex than that described in the  $z$  coordinate. Here,  $\Delta r$  is the size of the smallest grid element in the radial direction.  $\Delta r = \Delta z$  is used throughout

the simulation.  $i$  numbers the grid elements radially from the center of the electrode. By analogy to  $\Delta z_j$  and  $z_j$ ,  $\Delta r_i$  is the thickness of the  $i$ th radial element, and  $r_i$  is the distance radially from the center of the electrode to the point in the  $i$ th element where the concentration is represented. Because the radial grid expands, contracts, and expands, the calculation of  $\Delta r_i$  and  $r_i$  is more complex than the calculation of  $\Delta z_j$  and  $z_j$ . The calculations of these values are summarized in Table 1, where  $a = N_{ra}\Delta r$  and  $b = \sum_{i=1}^{N_{rb}} \Delta r_i$ .  $N_{ra}$  and  $N_{rb}$  are the number of grid elements across the radius of the active electrode area and the total electrode radius, respectively. The grid elements ( $\Delta r$ ) are of uniform size across the active electrode surface, while they vary in size across the insulator.

**Dimensionless Parameterization.** To make the simulation most general, the following dimensionless parameters are introduced. Total time,  $T_t$ , is divided into  $k_{\max}$  time steps, where each time step has a length  $\Delta t$ ;  $\Delta t = T_t/k_{\max}$ .  $k$  is the simulation time counter, such that for any time,  $t$ ,  $t = k\Delta t$ . The dimensionless simulation parameters are then

concentration

$$AA(j, i, k) = \frac{c_A(z, r, t)}{c_A^0} \quad (17)$$

time

$$\tau(k) = \frac{t}{T_t} = \frac{k}{k_{\max}} \quad (18)$$

potential

$$V(k) = \left\{ \begin{array}{ll} \frac{F}{RT} \left[ E_o + 2(E_t - E_o) \frac{k}{k_{\max}} \right] & 0 \leq k \leq k_{\max}/2 \\ \frac{F}{RT} \left[ E_o + 2(E_t - E_o) \left( 1 - \frac{k}{k_{\max}} \right) \right] & k_{\max}/2 < k \leq k_{\max} \end{array} \right\} \quad (19)$$

**Table 2. Dimensionless Diffusion Coefficients in Cylindrical EESG<sup>a</sup>**

simulation diffusion coefficient	real expression	simulation expression
DZ2( <i>j</i> )	$\frac{D\Delta t}{\Delta z_j} \frac{1}{[z_{j+1} - z_j]}$	$\frac{DM}{\text{Delt\_}z(j)} \frac{1}{[\text{Ave\_}z(j+1) - \text{Ave\_}z(j)]}$
DZ1( <i>j</i> )	$\frac{D\Delta t}{\Delta z_j} \frac{1}{[z_j - z_{j-1}]}$	$\frac{DM}{\text{Delt\_}z(j)} \frac{1}{[\text{Ave\_}z(j) - \text{Ave\_}z(j-1)]}$
DR2( <i>i</i> )	$\frac{D\Delta t}{\Delta r_i} \frac{1}{[r_{i+1} - r_i]}$	$\frac{DM}{\text{Delt\_}r(i)} \frac{1}{[\text{Ave\_}r(i+1) - \text{Ave\_}r(i)]}$
DR1( <i>i</i> )	$\frac{D\Delta t}{\Delta r_i} \frac{1}{[r_i - r_{i-1}]}$	$\frac{DM}{\text{Delt\_}r(i)} \frac{1}{[\text{Ave\_}r(i) - \text{Ave\_}r(i-1)]}$
DR3( <i>i</i> )	$\frac{D\Delta t}{r_i} \frac{1}{[r_{i+1} - r_{i-1}]}$	$\frac{DM}{\text{Ave\_}r(i)} \frac{1}{[\text{Ave\_}r(i+1) - \text{Ave\_}r(i-1)]}$

<sup>a</sup> DM =  $D\Delta t/\Delta z^2 = D\Delta t/\Delta r^2$ . Delt\_*z*(*j*) =  $\Delta z_j/\Delta z$  and Delt\_*r*(*i*) =  $\Delta r_i/\Delta r$ . Ave\_*z*(*j*) =  $z_j/\Delta z$  and Ave\_*r*(*i*) =  $r_i/\Delta r$ .

diffusion coefficient

$$DM = D \frac{\Delta t}{\Delta r^2} = D \frac{\Delta t}{\Delta z^2} \quad (20)$$

current

$$Z(k) = \frac{a\pi i(t)}{4nFADc_A^\circ} = \frac{i(t)}{4nFaDc_A^\circ} \quad (21)$$

where  $4nFaDc_A^\circ = i_{\text{disk},b \rightarrow \infty}^{\text{ss}}$ , the steady state, limiting current at a disk inlaid in a semiinfinite insulating plane.<sup>25</sup>

The finite difference representation of eq 2, based on a central difference in space and a forward difference in time is

$$\begin{aligned} c_A(z_j, r_i, t + \Delta t) = & c_A(z_j, r_i, t) + \\ & D_A \frac{\Delta t}{\Delta z} \left[ \frac{c_A(z_{j+1}, r_i, t) - c_A(z_j, r_i, t)}{z_{j+1} - z_j} - \frac{c_A(z_j, r_i, t) - c_A(z_{j-1}, r_i, t)}{z_j - z_{j-1}} \right] + \\ & D_A \frac{\Delta t}{\Delta r} \left[ \frac{c_A(z_j, r_{i+1}, t) - c_A(z_j, r_i, t)}{r_{i+1} - r_i} - \frac{c_A(z_j, r_i, t) - c_A(z_j, r_{i-1}, t)}{r_i - r_{i-1}} \right] + \\ & 2D_A \frac{\Delta t}{r_i} \left[ \frac{c_A(z_j, r_{i+1}, t) - c_A(z_j, r_{i-1}, t)}{r_{i+1} - r_{i-1}} \right] \quad (22) \end{aligned}$$

When the distance coordinates of *r* and *z* are converted to *i* and *j*, and time *t* is converted to *k*, the above equation can be simply written in dimensionless form as

$$\begin{aligned} AA(j, i, k+1) = & AA(j, i, k) + DZ2(j) [AA(j+1, i, k) - \\ & AA(j, i, k)] + DZ1(j) [AA(j, i, k) - AA(j-1, i, k)] + \\ & DR2(i) [AA(j, i+1, k) - AA(j, i, k)] + DR1(i) [AA(j, i, k) - \\ & AA(j, i-1, k)] + DR3(i) [AA(j, i+1, k) - AA(j, i-1, k)] \quad (23) \end{aligned}$$

DZ2(*j*), DZ1(*j*), DR2(*i*), DR1(*i*), and DR3(*i*) are coordinate-dependent, dimensionless parameters, which combine DM with either  $\Delta z_j$  and  $z_j$  or  $\Delta r_i$  and  $r_i$  and are defined as listed in Table 2. During each time step, eq 23 is evaluated for all *i* and *j*, subject to the initial and boundary conditions of eqs 5–14. The dimensionless current, *Z*(*k*), is then evaluated, as in eqs 3 and 21, by summing the flux normal to the electrode surface for *j* = 1 and *i* ≤ *N<sub>ra</sub>*.

All simulations were performed for *n* = 1, β = 0.3, and |*E<sub>f</sub>* − *E*<sup>o</sup>| = 0.250 V. The simulation was performed on a VAX-VMS 8600 cluster.

## RESULTS AND DISCUSSION

**Verification of Simulation Validity.** Simulations should be checked against any known limiting solution and for lack of variation in their output with further increases in their temporal and spatial resolution. The validity of this simulation was tested in several ways. First, the program was run with a uniform grid for both a potential step to the mass transport limit and cyclic voltammetry for two cases: linear diffusion (*a* → ∞) and an inlaid disk where *b* → ∞. The difference between the analytical solutions and simulation results was ≤ 0.05%.

Second, the nonuniform two-dimensional EESG was tested in several ways. Necessarily, the difference in the results of simulations based on the uniform grid and the one-dimensional regular EESG approaches zero as the number of time iterations becomes sufficiently large.<sup>19–22</sup> The one-dimensional, uniform EESG yielded the same result as the one-dimensional uniform grid for the case of linear diffusion to a planar electrode. (The simulation is restricted to linear diffusion by placing simulation elements directly over the electrode; no elements are placed over the insulator. Essentially, the simulation is for a disk in a well.) To ensure that two-dimensional problems were well simulated by the program, the one- and two-dimensional uniform EESG methods were applied to the disk in a well, yielding the same results within the limits of the simulation (±0.05%). To test whether the two-dimensional, nonuniform EESG yielded a valid result, the two-dimensional uniform and nonuniform EESGs were compared for a disk with a semiinfinite shield. The results were the same within the limitations of simulation, and both yielded the expected steady state current,  $i_{\text{disk},b \rightarrow \infty}^{\text{ss}} = 4nFaDc_A^\circ$ .

Third, in evaluating a simulation, it is important to verify that the temporal and spatial resolution is sufficient. To optimize the spatial resolution, the simulation was run with increasing *N<sub>ra</sub>*, the number of elements across the electrode surface. *N<sub>ra</sub>* was considered optimized when further increases in *N<sub>ra</sub>* did not significantly change the simulated current. The results of the simulation for a disk inlaid in an infinite insulating plane are shown in Table 3 for *k<sub>max</sub>* = 2.88 × 10<sup>5</sup>, and 1 ≤ *N<sub>ra</sub>* ≤ 7. Theoretically,

(25) Saito, Y. *Rev. Polarogr.* **1968**, *15*, 177.

**Table 3. Resolution of the Dimensionless Steady State Current ( $Z_{ss}$ ) as a Function of Increasing Number of Grid Elements across the Electrode Surface ( $N_{ra}$ ): Simulation for an Inlaid Disk in a Semiinfinite Plane, Where Theoretically,  $Z_{ss} = 1$ .  $k_{max} = 2.88 \times 10^5$ .**

$N_{ra}$	$Z_{ss}$	100 (1 - $Z_{ss}$ )	$N_{ra}$	$Z_{ss}$	100 (1 - $Z_{ss}$ )
1	0.752 13	24.8	5	0.991 54	0.85
2	0.916 24	8.51	6	0.999 80	0.02
3	0.958 77	4.12	7	1.000 08	-0.008
4	0.979 69	2.03			

the dimensionless steady state current,  $Z_{ss}$ , for this case should be 1. From Table 3, the resolution improves as the number of grid elements increases. However, each time  $N_{ra}$  increases by 1, the computation time increases 2 orders of magnitude. In all of the following simulations,  $N_{ra}$  was chosen as 6 because this was sufficient to reduce the variation in the simulated response to below 0.05% despite further increases in  $N_{ra}$  and still allow the simulation to run in a reasonable amount of time.  $k_{max}$  was chosen in another set of simulations for the same problem, where  $N_{ra} = 6$ , and  $k_{max}$  was increased until  $Z_{ss}$  equaled the theoretical value within 0.02%.

**General Considerations in Relating Simulation and Experimental Results.** The simulation is used to characterize the cyclic voltammetric response for microelectrodes as a function of scan rate and  $b/a$ . The voltammetric results can be understood in terms of the following points. First, for microdisks, independent of the shield thickness, steady state is achieved when the limiting current is scan rate independent, and the current normalized by the limiting current equals  $[1 + \exp(nF(E - E^\circ)/RT)]^{-1}$ . (This equality assumes equal diffusion coefficients.) That is, for any electrode limited solely by reversible electron transfer kinetics, the current is characterized by the Nernst equation. Second, steady state voltammograms are recognized by the superposition of the forward and reverse branches of the sigmoidal voltammogram. Third, for  $b \rightarrow \infty$ , Oldham, Zoski and co-workers<sup>26-28</sup> characterized the approach to steady state based on  $\Delta E_{1/2}$ , the separation between the forward and reverse branches measured at half the steady state, limiting current.  $\Delta E_{1/2}$  is also used to characterize the approach to steady state for microdisks with finite shields. Fourth, the voltammetric response of any microdisk can be understood in terms of  $a$ ,  $b$ , and the growth of the diffusion layer with decreasing scan rate. If the diffusion layer thickness is small compared to  $a$  and  $b$ , the voltammogram will be governed by linear diffusion. If the diffusion length is greater than  $a$ , but less than  $b$ , flux to the electrode will only be established from above the plane of the electrode and a hemispherical diffusion profile will tend to form. The voltammetric response will be the same as that of a disk in an infinite insulating plane. If the diffusion length is larger than  $a$  and  $b$ , flux to the electrode will be established from both above and below the plane of the electrode, and a roughly spherical diffusion profile will tend to form. As the scan rate is decreased, radial flux to the electrode will increase relative to linear flux and the voltammogram will become increasingly sigmoidal. At sufficiently slow scan rates,

steady state will be approached. Fifth, for a microdisk, once the diffusion length is  $\geq a$ , the shape of the voltammogram will be determined by the relative contributions of linear and radial diffusion and whether the radial component is established below the plane of the electrode or not. Sixth, as  $b/a$  decreases, more flux is provided from behind the plane of the electrode at a given scan rate. Seventh, because the total flux is enhanced by diffusion from behind the plane of the electrode, the steady state current increases as  $b$  decreases. Electrodes with finite shields have higher limiting currents than electrodes of the same size in infinite shields. Eighth, we define the onset of the approach to steady state as when there is no discernible peak current in the cyclic voltammogram. Because of higher flux associated with diffusion from behind the plane of the electrode, steady state is achieved more rapidly with finite than infinite shields.

The purpose of this study is to investigate the cyclic voltammetric response with scan rate for a wide range of  $b/a$  values and to provide a method for determining  $a$  and  $b$ . The response is examined from the linear diffusion regime observed at high scan rates to the radial diffusion regime observed at steady state and slow scan rates. The critical parameters are the characteristic lengths,  $a$  and  $b$ , and the scan rate,  $v$ . It will be easier to interpret the results of the simulation if the scan rate is reduced to a length,  $\delta$ ,

$$\delta = [RTD/nFv]^{1/2} \quad (24)$$

$4a^2/\delta^2$ , the "sphericity factor", has been used to characterize<sup>26,27</sup> the approach to steady state when  $b \rightarrow \infty$ . To compare any experimental data to the simulated results of this paper, calculate  $\delta$  by substituting the experimental  $D$ ,  $T$ , and  $v$  into eq 24.

Let us emphasize that the full parametrization of the voltammetric responses at microelectrodes requires consideration of another length parameter, the diffusion length,  $l$ , established at the time the applied potential is equal to the switching potential,  $E_f$ .

$$l = [D|E_f - E^\circ|/v]^{1/2} \quad (25)$$

The following discussion is limited to  $|E_f - E^\circ| = 0.250$  V. In general, the effects of switching potential will be less substantial as the system approaches steady state. In applying the methods to determine  $a$  and  $b$  outlined in this paper, make all measurements with the switching potential 250 mV past  $E^\circ$ .

Oldham and Zoski<sup>13</sup> have shown that, under reversible electron transfer conditions, the steady state currents at a hemispherical electrode and an inlaid disk in a semiinfinite insulating shield are equal if an appropriate area correction is introduced. The "superficial diameter" of a hemispherical electrode is  $\pi r_o$ , where  $r_o$  is the radius of the hemisphere. The steady state, limiting current at a hemisphere electrode embedded in a semiinfinite insulating plane is

$$i_{\text{hemisphere}}^{\text{ss}} = \pi n F r_o D c_A^\circ \quad (26)$$

The diameter (and superficial diameter) of an inlaid disk is  $2a$ , where  $a$  is the radius of the disk; the steady state, limiting current for a planar electrode, again embedded in a semiinfinite insulating plane, is

$$i_{\text{disk}, b \rightarrow \infty}^{\text{ss}} = 4nFaDc_A^\circ \quad (27)$$

For  $r_o = a$ ,  $(4/\pi)i_{\text{hemisphere}}^{\text{ss}} = i_{\text{disk}, b \rightarrow \infty}^{\text{ss}}$ . All simulated currents are

(26) Zoski, C. G.; Bond, A. M.; Colyer, C. L.; Myland, J. C.; Oldham, K. B. *J. Electroanal. Chem.* **1989**, *263*, 1-21.

(27) Zoski, C. G. *J. Electroanal. Chem.* **1990**, *296*, 317-333.

(28) Zoski, C. G.; Bond, A. M.; Allinson, E. T.; Oldham, K. B. *Anal. Chem.* **1990**, *62*, 37-45.

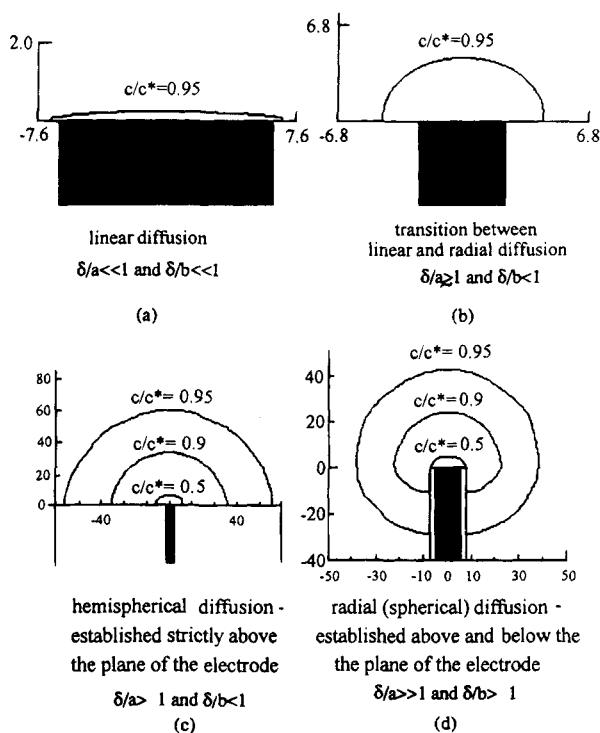


**Figure 2.** Concentration profiles for various transport regimes possible at microelectrodes. The nature of the transport regimes established at microelectrodes is determined by the relationship between the scan rate parameter ( $\delta$ ) and the characteristic lengths,  $a$  and  $b$ . Parts a–d correspond to increasing  $\delta$  (decreasing  $\nu$ ). Concentration contours, determined by simulation, are shown for various values of  $c(r, z, t)/c_A^\infty$ , denoted  $c/c^*$  in the figure. As in Figure 1, the blackened portion of the figure is the cross section of the electrode. The numbers of the axes are dimensionless distances; each electrode has a radius of six dimensionless units. (a) and (b) are for shields effectively semiinfinite; (c) and (d) have wide and narrow shields, respectively. (a) Linear diffusion regime. (b) Regime of transition between linear and radial diffusion. (c) Hemispherical diffusion, where the diffusion profile is established solely above the plane of the electrode. (d) Radial diffusion, where a roughly spherical diffusion profiles is established by radial diffusion above and below the plane of the electrode.

made dimensionless by  $(4/\pi)i_{\text{hemisphere}}^{\text{ss}}$ , the area corrected hemisphere current; from eq 21,  $Z(k) = i(t)/4nFac_A^\infty = i(t)/[(4/\pi)i_{\text{hemisphere}}^{\text{ss}}]$ .  $Z(k)$  is the current normalized to the steady state, limiting current for a planar electrode embedded in a semiinfinite insulating plane. If transport is limited to radial diffusion above the plane of the electrode ( $b/a \rightarrow \infty$ ),  $Z(k) = 1$ , and a hemispherical diffusion profile is established. If transport occurs from behind the plane of the electrode ( $b/a < \infty$ ), the diffusion field will be more spherical and  $Z(k) > 1$ . The error introduced by using the area-corrected hemisphere current equation for a disk with a finite shield is characterized by the extent to which  $Z(k)$  exceeds 1.

The range of responses for reversible electrode kinetics and  $|E_f - E^\circ| = 0.250$  V is characterized by two dimensionless length ratios:  $\delta/a$  and  $\delta/b$ . (Complete parameterization of the system requires consideration of the switching potential, which is not included here.) Three transport regimes are possible, and the diffusion profiles associated with each regime are shown in Figure 2. The linear transport regime is characterized by  $\delta/a \ll 1$  (Figure 2a). The other transport regimes are characterized by radial diffusion. The first radial transport regime occurs when the diffusion field is established solely above the plane of the

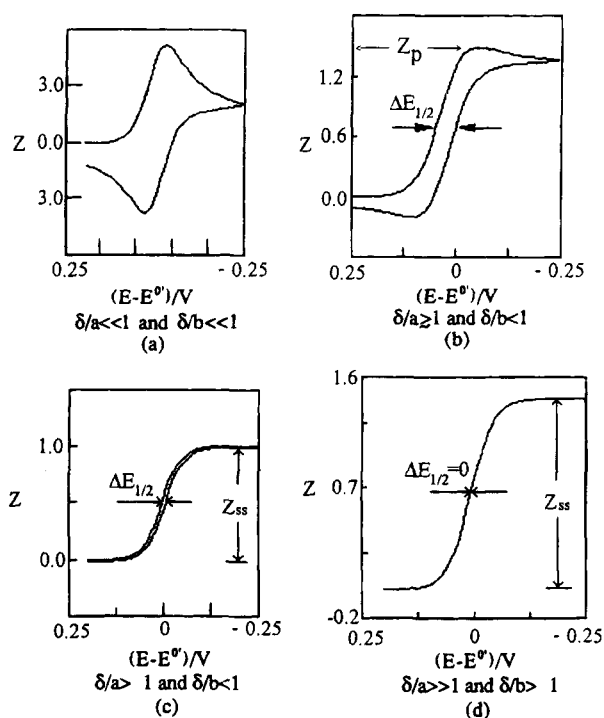


**Figure 3.** Cyclic voltammetric responses for the transport regimes shown in Figure 2. Three experimentally significant parameters,  $Z_{\text{ss}}$  ( $i_{\text{ss}}$ ),  $\Delta E_{1/2}$ , and  $Z_p$  ( $i_p$ ), are shown. (a) Linear transport regime observed when  $\delta/a \ll 1$ ; cyclic voltammogram identical to that observed for a large planar electrode. (b) Regime of transition between linear and radial diffusion; voltammogram shows  $\Delta E_{1/2} > 0$  (indicative of not yet being at steady state) and a discernible peak current,  $Z_p$ . (c) Hemispherical diffusion exhibits a small but nonzero  $\Delta E_{1/2}$ , no peak current, and  $Z_{\text{ss}} = 1$ . (d) Radial diffusion established above and below the plane of the electrode leads to  $\Delta E_{1/2} = 0$  (steady state), no peak current, and  $Z_{\text{ss}} > 1$ .

electrode,  $\delta/b < 1$ . There are two cases to consider:  $\delta/a \geq 1$  and  $\delta/a > 1$ , shown in Figure 2b and c, respectively. When  $\delta/a > 1$ , hemispherical diffusion is established above the plane of the electrode (Figure 2c). When  $\delta/a \geq 1$ , the diffusion field is in transition between the linear diffusion (Figure 2a) and the hemispherical diffusion (Figure 2c), as shown in Figure 2b. The regime of transition is of interest in determining  $a$  and  $b$ . The second radial transport regime is established when  $\delta/b > 1$ , and the diffusion field is established radially above and below the plane of the electrode and approaches a spherical profile (Figure 2d). Whether both hemispherical and spherical diffusion zones are observed depends on the relative values of  $b$  and  $a$ . However, except possibly when  $a \ll b$ , and  $b < 2 \mu\text{m}$ , the range of scan rates needed to observe both hemispherical and spherical diffusion is too broad to be experimentally accessible because of natural convection. The issue of the scan rate needed to reach steady state when  $b \rightarrow \infty$  has been addressed.<sup>26–28</sup>

The simulated cyclic voltammetric responses for each of these transport regimes are shown in Figure 3. The normal voltammetric response for linear diffusion is shown in Figure 3a, where  $\delta/a \ll 1$ . The transitional response between linear and radial diffusion, shown in Figure 3b, is characterized by a discernible peak current and narrowing along the potential axis between the forward and reverse branches of the voltammogram. The sigmoidal responses expected for radial transport processes are shown in Figure 3c and d. The limiting current is greater when radial diffusion is established above and below the plane of the



electrode (Figure 3d) rather than just above (Figure 3c). Steady state is characterized by superposition of the forward and reverse branches. At the scan rate used to generate Figure 3, the finite shield electrode (Figure 3d) is at steady state, but the response for  $b \rightarrow \infty$  is not (Figure 3c). At a slower scan rate, the branches would superimpose for  $b \rightarrow \infty$  as well. Steady state is achieved more rapidly (at lower  $\delta$ , higher  $\nu$ ) when diffusion is established above and below the plane of the electrode.

Three experimental observables are useful in characterizing the geometric parameters of these microelectrodes. The steady state, limiting current,  $i_{ss}$ , is scan rate independent and occurs when steady state, radial diffusion is established.  $i_{ss} = (4/\pi)i_{\text{hemisphere}}^{ss}$  if hemispherical diffusion has been established, as in Figure 2c, and  $i_{ss} > (4/\pi)i_{\text{hemisphere}}^{ss}$  if steady state diffusion has been established above and below the plane of the electrode (Figure 2d). The higher current arises from the additional flux from behind the plane of the electrode.  $i_{ss}$  is analogous to the dimensionless current,  $Z_{ss}$ , shown in Figure 3c and d. Whether steady state has been achieved and whether it is governed by hemispherical or spherical diffusion can be determined from  $\Delta E_{1/2}$ , the difference in potential observed on the forward and reverse branches of a cyclic voltammogram when the current is half the current at the switching potential. On the approach to steady state, this current is  $i_{ss}/2$ . As steady state is approached,  $\Delta E_{1/2} \rightarrow 0$ .  $\Delta E_{1/2}$  approaches zero more rapidly under spherical (Figure 2d) than hemispherical conditions (Figure 2c). The peak current,  $i_p$ , is observed before the response reaches steady state, as illustrated in Figure 3b where,  $i_p = Z_p 4nFADc_A^\circ$ . The presence of  $i_p$  and  $\Delta E_{1/2} > 0$  means the system is not at steady state.

Results are presented for various values of  $b/a$ . The discussion will be broken down into two cases: the finite disk electrode in a semiinfinite shield ( $\delta/b < 1$ ) and the finite disk electrode in a finite shield ( $\delta/b > 1$ ). Note, as long as  $\delta/b < 1$ , the voltammetric response will be that for an electrode within a semiinfinite shield, and the shape of the diffusion field will approach a hemisphere. As  $\delta/b$  exceeds 1, diffusion from behind the plane of the electrode contributes to the flux, and the diffusion field will approach a sphere.

#### Disk of Finite Radius in a Shield of Infinite Thickness.

The cyclic voltammetric approach to steady state and the steady state response of disks inlaid in infinite insulating planes has been ably addressed by Oldham, Zoski and co-workers.<sup>26,27,29,30</sup> The simulation of this transition is shown in Figures 2a–c and 3a–c, as  $\delta/a$  increases ( $\nu$  decreases). The residual peak associated with the linear diffusion process observed in Figure 3b is gone in Figure 3c, where the maximum current is  $i_{ss}$  ( $Z_{ss} = 1$ ) but  $\Delta E_{1/2} > 0$ .

We define the onset of the approach to steady state as when the peak current has been reduced to the current at the switching potential;  $\Delta E_{1/2} > 0$ . For purposes of the simulation, this was taken to be when  $Z_p$  was within 1% of  $Z_{ss}$  and  $Z_{ss} \leq 1.01$ . From Zoski and co-workers,<sup>26,27,29,30</sup> the peak current constraint is met for  $\delta/a \geq 0.5$ , while  $\Delta E_{1/2}$  will be greater than zero until  $\delta/a > 40$ . Once  $Z_p = Z_{ss} \leq 1.01$ ,  $\nu$  will have to be reduced roughly 2 orders of magnitude before  $\Delta E_{1/2} = 0$ . This long transition to the steady state is characteristic of a semiinfinite shield.

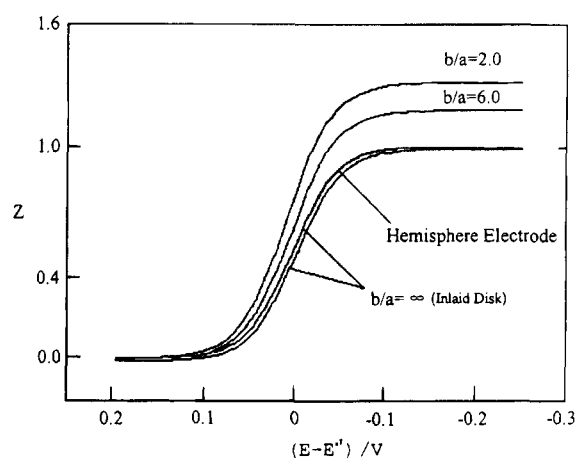


**Figure 4.** Cyclic voltammetric responses for a hemispherical electrode and inlaid disks where  $b/a \rightarrow \infty$  and  $b/a = 6.0$  and  $2.0$ ;  $\delta/a = 8.5$ . A hemisphere electrode of radius  $r_0 = 4a/\pi$  yields a voltammogram with the forward and reverse branches superimposed. An inlaid disk in a semiinfinite shield yields a forward sweep which superimposes on the voltammogram for the hemisphere electrode with an equivalent corrected area. The reverse sweep is slightly offset and shifted to more negative potentials, as expected when  $\delta/a$  is too small to be at steady state. The disks with finite shields yield limiting currents that are larger than the hemisphere electrode and that increase with decreasing shield thickness. For the finite shields, the forward and reverse branches superimpose, as expected at steady state. The finite shield electrodes achieve steady state at smaller  $\delta/a$  (higher  $\nu$ ) than required for  $b \rightarrow \infty$ .

Hemispherical diffusion ( $\delta/b < 1$ ) is identified by (1)  $i_{ss}$  equal to the area-corrected hemisphere current and (2) the slow approach of  $\Delta E_{1/2} \rightarrow 0$  with  $\delta/a$  once the current peak is no longer discernible. If a microdisk can be driven into the hemispherical diffusion regime, where  $\delta/b < 1$ , then the electrode radius,  $a$ , is readily determined from the steady state current,  $a = i_{ss}/4nFDc_A^\circ$ . Alternatively, if the cyclic voltammetric responses can be driven into a linear diffusion regime where  $\delta \ll a$ ,  $a$  can be found from the peak current expression developed by Nicholson and Shain<sup>31</sup>

$$i_p = 0.4463nF\pi a^2 c_A^\circ [DnF\nu/RT]^{1/2} \quad (28)$$

where a plot of  $i_p$  versus  $\nu^{-1/2}$  will be linear with zero intercept. If this method is used, verify the experimentally determined value of  $a > l$  (eq 25) at the smallest  $\nu$ . If  $\delta \ll a$ , then eq 28 applies whether  $b$  is infinite or not.

#### Disk of Finite Radius in a Shield of Finite Thickness.

When  $b/a$  is not infinite, diffusion from behind the plane of the electrode can contribute to the flux at the electrode surface. This affects  $i_{ss}$ ,  $i_p$ , and  $\Delta E_{1/2}$ , as discussed below.

**$i_{ss}$ .** The cyclic voltammetric responses for three inlaid disks ( $b/a = 2.0, 6.0$  and  $\infty$ ) and a hemispherical electrode are shown in Figure 4 for  $\delta/a = 8.5$ . When  $b/a \rightarrow \infty$ , the forward branch superimposes on the response for a hemispherical electrode and achieves  $Z_{ss} = 1$ , but the reverse branch is shifted to slightly negative potentials.  $\Delta E_{1/2} \neq 0$  because the diffusion field is not yet at steady state. For  $b/a = 2$  and  $6$ ,  $\Delta E_{1/2} = 0$ , consistent with a steady state diffusion profile established above and below the plane of the electrode (Figure 2d). Steady state is achieved at smaller  $\delta/a$  (higher  $\nu$ ) for the finitely shielded electrodes because flux from above and below the plane of the electrode contributes

(29) Bond, A. M.; Oldham, K. B.; Zoski, C. G. *J. Electroanal. Chem.* **1988**, *245*, 71–104.

(30) Oldham, K. B. *J. Electroanal. Chem.* **1989**, *260*, 461–467.

(31) Nicholson, R. S.; Shain, I. *Anal. Chem.* **1964**, *36*, 706.

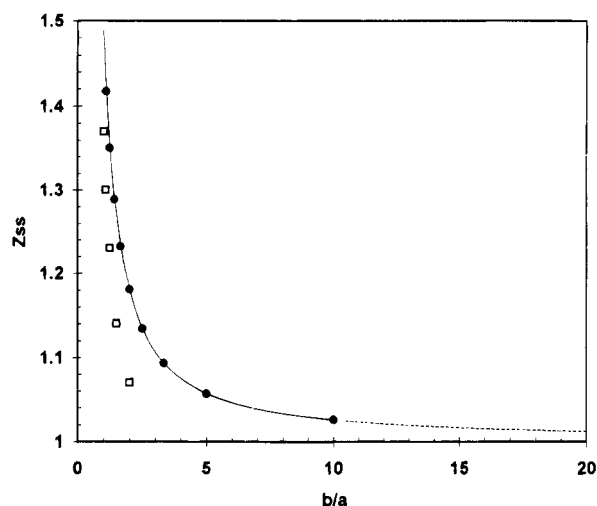


**Figure 5.** Increase in the steady state dimensionless current as the shield thickness decreases relative to the disk radius. Solid points are the results for the EESG; open points are from ref 18. As  $b/a$  approaches  $\infty$ , the system is a disk in a semiinfinite insulating plane, and the steady state current approaches the area-corrected hemispherical steady state current. As  $b/a$  approaches 1, the shield approaches zero thickness, and the steady state current approaches  $1.489 i_{\text{hemisphere}}^{\text{ss}}$  (solid points). The solid line is the fit of eq 29.

to establish the radial diffusion profile. At steady state, for all electrodes, the current response is governed solely by the Nernst equation.

At steady state,  $i_{\text{ss}}$  increases as  $b/a$  decreases, consistent with increasingly effective flux from behind the plane of the electrode. As  $b$  shrinks relative to  $a$ , flux around the edges of the insulator to the edges of the electrode becomes increasingly radial and, therefore, higher. This is illustrated in Figure 5. As  $b/a \rightarrow \infty$ ,  $Z_{\text{ss}} \rightarrow 1$ , and in the limit of  $b \rightarrow a$ ,  $Z_{\text{ss}} \rightarrow 1.489$ . These results are consistent with  $Z_{\text{ss}}$  for a disk in a finite insulator lying between the  $Z_{\text{ss}}$  for a spherical electrode ( $Z_{\text{ss}} = 2$ ) and for a disk with an infinite shield ( $Z_{\text{ss}} = 1$ ).  $i_{\text{ss}}$  can be as much as 1.489 times the current predicted by the area-corrected hemispherical current or  $1.896 i_{\text{hemisphere}}^{\text{ss}}$ . Thus, a substantial error can result when the equation for the area-corrected hemisphere current is used to calculate the current response for a disk in a thin shield.

The solid points in Figure 5 were generated by the EESG. For comparison, the steady state flux found with a fixed grid hopscotch algorithm by Shoup and Szabo<sup>18</sup> for chronoamperometry is shown as open points. The fixed grid consistently yields a lower steady state current than the EESG; in the limit of  $b/a \rightarrow 1$ ,  $Z_{\text{ss}} = 1.39$ . The lower values of  $Z_{\text{ss}}$  probably reflect the less effective resolution of the concentration gradients about the electrode/insulator and insulator/solution interfaces with the fixed grid. Shoup and Szabo noted this limitation in their simulation. In the EESG, more grid elements were placed at the interfaces where the concentration gradients are steepest, and the simulation spatial and temporal grids were made finer until no change in the output was observed with further increases in resolution. Shoup and Szabo generated the first reasonable approximation to the steady state current at finitely shielded electrodes, but the results generated here are probably more accurate.

$i_p$ .  $Z_p$  is shown in Figure 6 for various values of  $\delta/a$  and  $b/a$ . On the plots, the small arrows ( $\downarrow$ ) indicate the point at which  $b = l$  (eq 25). To the right of the small arrows, diffusion is restricted to above the plane of the electrode ( $b > l$ ). For any value of  $b/a$

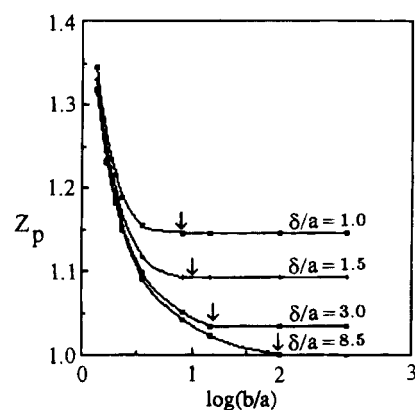


**Figure 6.** Transition of  $Z_p$  between steady state behavior and dependence on the scan rate. Steady state is at the left, where  $Z_p$  is independent of  $\delta/a$ . At the arrows ( $\downarrow$ ),  $b = l$ , the diffusion length. To the left of the arrows, diffusion from below the plane of the electrode contributes to the flux. To the right of the arrows, diffusion is confined above the plane of the electrode, and the peak current is dependent on the scan rate,  $\delta/a$ ; for a given  $a$ , as  $\delta/a$  increases ( $v$  decreases),  $Z_p$  decreases, and steady state is achieved when  $Z_p = Z_{\text{ss}} = 1$ .

in this regime,  $Z_p$  decreases with increasing  $\delta/a$  (decreasing  $v$ ) until  $\delta \gg a$ , where  $Z_p = Z_{\text{ss}} = 1$ , but the system will not be at steady state until  $\Delta E_{1/2} = 0$ . All points to the left of the small arrows ( $b < l$ ) in Figure 6 have some component of radial diffusion from behind the plane of the electrode. As  $b/a$  decreases, this flux component contributes an increasing fraction of the total flux to the electrode and the diffusion field is increasingly spherical. For a given scan rate ( $\delta/a$ ),  $Z_p$  increases as  $b/a$  decreases. This is expected as the system moves from a roughly hemispherical diffusion profile toward a spherical one. For small values of  $b/a$ ,  $Z_p$  is scan rate ( $\delta/a$ ) independent, and  $Z_p = Z_{\text{ss}}$ . From the convergence of the curves at small  $b/a$ , the onset of scan rate independence occurs when  $\delta/a \sim b/a$  or  $\delta \sim b$ . As  $b/a$  decreases, the system approaches steady state at smaller  $\delta/a$  (higher  $v$ ); the greater the flux from behind the plane of the electrode, the more quickly the system is driven to steady state. The smaller the  $b/a$ , the smaller the scan rate window where the transition  $i_p \rightarrow i_{\text{ss}}$  and  $\Delta E_p \rightarrow 0$  are observable.

$\Delta E_{1/2}$ . Steady state is achieved when  $\Delta E_{1/2} = 0$ . The variation of  $\Delta E_{1/2}$  with  $\delta/a$  and  $b/a$  is shown in Figure 7. Again, all the data to the right of the small arrows corresponds to a condition where  $b > l$ . When  $b > l$ ,  $\Delta E_{1/2}$  decreases as  $\delta/a$  increases ( $v$  decreases); the decrease is linear in  $(\delta/a)^{-1}$  for  $4 \text{ mV} < \Delta E_{1/2} < 28 \text{ mV}$ . To the left of the small arrows, some fraction of the total flux to the electrode comes from behind the plane of the electrode. As  $b/a$  decreases for fixed  $\delta/a$ , an increasing fraction of the flux is from behind the plane of the electrode and the system has an increasingly spherical diffusion profile, and  $\Delta E_{1/2}$  decreases. For a given value of  $b/a$ ,  $\Delta E_{1/2}$  decreases as  $\delta/a$  increases ( $v$  decreases) as the system passes from linear to spherical diffusion. Again,  $\Delta E_{1/2}$  decreases linearly with  $(\delta/a)^{-1}$  for  $4 \text{ mV} < \Delta E_{1/2} < 28 \text{ mV}$ . As  $b/a$  decreases, the system approaches spherical diffusion at smaller  $\delta/a$  (higher  $v$ ) because substantial flux from behind the plane of the electrode decreases the time required for transition from linear to radial diffusion. For finitely shielded electrodes, voltammograms approach steady state ( $\Delta E_{1/2} \rightarrow 0$ ) more rapidly than electrodes with infinite shields. Once  $i_p \rightarrow i_{\text{ss}}$ , the transition to steady state will be achieved when the scan rate has been decreased roughly 1 order of magnitude, as compared to 2 orders when  $b \rightarrow \infty$ .

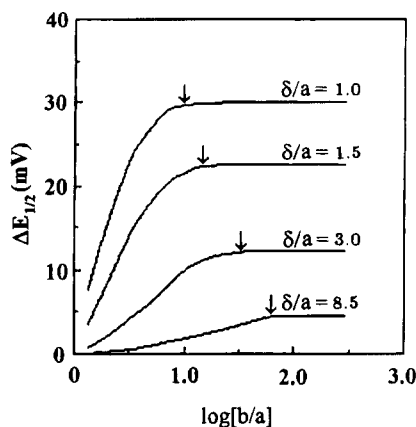


**Figure 7.**  $\Delta E_{1/2}$ , hysteresis of the forward and reverse branches of the cyclic voltammogram. As in Figure 6, the arrows indicate  $b = l$ . To the right of the arrows, the diffusion field is confined above the electrode, and  $\Delta E_{1/2}$  decreases as  $\delta/a$  increases ( $v$  decreases). To the left of the arrows, diffusion from behind the plane of the electrode contributes to the flux, and as  $\delta/a$  increases ( $v$  decreases),  $\Delta E_{1/2}$  approaches zero, consistent with a spherical diffusion profile. Steady state ( $\Delta E_{1/2} = 0$ ) is achieved more rapidly as  $b/a$  decreases.

In principle, for  $a \ll b$ , the voltammetric response can reach a quasi-steady state when  $\delta$  is sufficiently large compared to  $a$  to establish radial transport from above the plane of the electrode, but  $\delta < b$ . For longer diffusion lengths (slower scan rates),  $\delta$  may exceed  $b$ , and a second transition will be observed. When  $\delta$  is large compared to  $b$ , the true steady state will be observed with radial diffusion established above and below the plane of the electrode. The hemispherical regime is then a quasi-steady state. Because the time scales necessary to observe two scan rate independent regimes are sufficiently long, the observation of both regimes is unlikely unless  $a$  is less than a few tenths micrometers and  $b/a$  is about 50. It has been shown<sup>26,27</sup> that the time to achieve steady state within 2% for  $b \rightarrow \infty$  corresponds to  $\delta/a \sim 40$ . If  $b/a \sim 50$ , the onset of the transition to a spherical steady state would be  $\delta/a \sim 50$ . Steady state would be achieved when the scan rate was reduced roughly another order of magnitude.

**Methods for Determining  $a$  and  $b$  for Inlaid Microdisk Electrodes.** The simulation results provide several methods to determine  $a$  and  $b$  for an inlaid microdisk electrode. The choice of an appropriate method will depend on whether the experimentalist already knows  $a$  and how precisely the values of  $a$  and  $b$  must be known. Recall the methods are applicable for reversible electrode kinetics and a switching potential 0.250 V past  $E^\circ$ .

**$a$  is Known.**  $Z_{ss}$  generated by the simulation are shown as solid points in Figure 5. The line is the fit of  $i_{ss, \text{inlaid}}/4naFDc_A^\circ$  to  $b/a$  as

$$\frac{i_{ss, \text{inlaid}}}{4naFDc_A^\circ} = 1.000 + 0.234 \left[ \frac{b}{a} \right]^{-1} + 0.255 \left[ \frac{b}{a} \right]^{-2} \quad (29)$$

$R = 0.9999$

The dotted portion of the line is the extrapolation of this equation toward  $b/a \rightarrow \infty$ . For eq 29, when  $b/a \rightarrow \infty$ ,  $Z_{ss} \rightarrow 1$ . If  $a$  is known and the system can be driven to steady state,  $b$  is readily determined from the steady state current.  $a$  may be known from the diameter of the conductor used to form the electrode or  $a$  can be determined if the electrode can be scanned fast enough to establish linear diffusion (eq 28).

**Both  $a$  and  $b$  Are Unknown.** If neither  $a$  nor  $b$  is known, the relationships developed below will be useful. The method

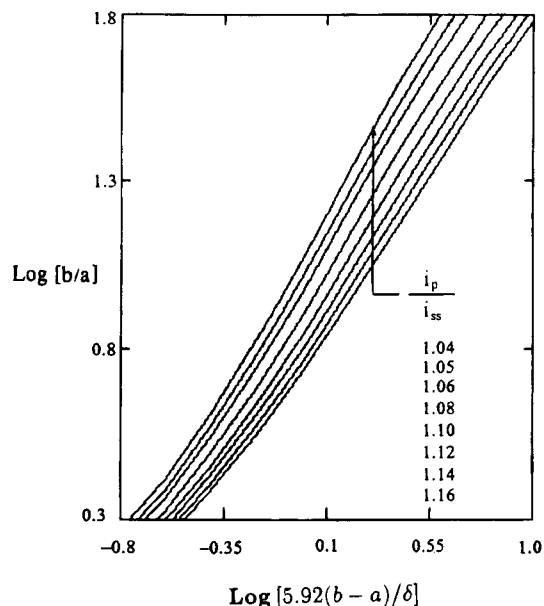


**Figure 8.** Working curves to determine  $b/a$  and  $b - a$ . Two working curves are identified by varying  $\delta$  to find two ratios of  $i_p/i_{ss}$  among those listed on the plot. Once the two working curves are identified, a straight edge held parallel to the  $x$  axis is moved down the plot until the separation between the two curves is  $\log[\delta_2/\delta_1]$ . At this point, the value on the  $y$  axis is  $b/a$ . The value of  $b - a$  is found on the  $x$  axis from one of the working curves. An analytical evaluation of  $b$  and  $a$  is described in the text.

uses both steady state and nonsteady state data and applies for  $|E_f - E^\circ| = 0.250$  V. The relationship relies on values of  $i_p$  and  $i_{ss}$  and is parameterized by  $i_p/i_{ss}$ ,  $b/a$ , and  $\delta$ . The working curves (Figure 8) show the ratio of  $i_p/i_{ss}$  at two scan rates ( $\delta_1$  and  $\delta_2$ ) and can be used to find  $b/a$  and  $(b - a)/\delta$ .  $i_{ss}$  can be measured directly at sufficiently slow scan rates. Cyclic voltammograms are then recorded at two scan rates,  $v_1$  and  $v_2$ , both fast enough that  $i_p > i_{ss}$ . Let  $R_1 = i_{p1}/i_{ss}$  at  $v_1$ , and  $R_2 = i_{p2}/i_{ss}$  at  $v_2$ .  $v_1$  and  $v_2$  are varied until  $R_1$  and  $R_2$  are each one of the ratios shown in Figure 8: 1.04, 1.05, 1.06, 1.08, 1.10, 1.12, 1.14, and 1.16. Then,  $a$  and  $b$  can be found either by using a working curve or by using an analytical method. The choice of an analytical method will depend on how large  $a/b$  is.

Consider the working curve method first. The values of  $R_1$  and  $R_2$  identify the two appropriate working curves in Figure 8.  $\delta_1$  and  $\delta_2$  are known for these curves. Note,  $\log[1/\delta_1] - \log[1/\delta_2] = \log[5.9193(b - a)/\delta_1] - \log[5.9193(b - a)/\delta_2]$ . For a given value of  $b - a$ , the working curves associated with  $R_1$  and  $R_2$  should be separated by  $\log[1/\delta_1] - \log[1/\delta_2]$ . With a straight edge parallel to the  $x$  axis, slide down the working curves until they are separated by  $\log[\delta_2/\delta_1]$ . At this point, the value of the  $y$  axis corresponds to  $\log[b/a]$ , and the value on the  $x$  axis for, say  $R_1$ , corresponds to  $\log[5.9193(b - a)/\delta_1]$ . The  $R_2$  curve could be used as well.  $b/a$  can also be substituted into eq 29 to find  $a$ . With this information,  $b$  and  $a$  can be determined.

Now, consider the analytical methods. The data shown in Figure 8 can be fit to polynomials, which can be used to find  $b/a$  and  $b - a$ . As for the working curve method, two sets of experimental data ( $R_1$  and  $R_2$ , and the associated  $\delta_1$  and  $\delta_2$ ) are needed because two parameters must be separated. Appropriate values of values  $R_1$  and  $R_2$  are found. These are used to find the set of coefficients appropriate to each expression of the polynomial. With the two sets of coefficients and  $\delta_1$  and  $\delta_2$ , two polynomials

**Table 4. Parameters To Evaluate  $b/a$  and  $b - a$  According to the Quadratic Equation 30: Relative Error  $\leq 2.5\%$ ; Appropriate for  $b/a \leq 14.55$**

$i_p/i_{ss}$	$A_2$	$A_1$	$A_0$
1.04	0.481 67	1.380 04	1.076 44
1.05	0.463 86	1.318 63	1.018 02
1.06	0.444 54	1.263 48	0.969 87
1.08	0.406 61	1.170 41	0.894 46
1.10	0.373 34	1.098 21	0.837 80
1.12	0.211 13	1.022 95	0.806 37
1.14	0.194 98	0.989 95	0.770 12
1.16	0.184 52	0.963 86	0.738 90

**Table 5. Parameters To Evaluate  $b/a$  and  $b - a$  According to the Cubic Equation 31: Relative Error  $\leq 0.5\%$ ; Appropriate for  $b/a \leq 63$**

$i_p/i_{ss}$	$B_3$	$B_2$	$B_1$	$B_0$
1.04	-0.226 49	0.0965 12	1.235 9	1.076 4
1.05	-0.229 57	0.104 48	1.206 8	1.024 1
1.06	-0.226 79	0.116 79	1.180 8	0.980 00
1.08	-0.212 04	0.143 36	1.133 0	0.908 36
1.10	-0.194 45	0.164 97	1.090 4	0.852 17
1.12	-0.145 97	0.160 00	1.042 47	0.808 95
1.14	-0.127 47	0.164 23	1.010 42	0.771 76
1.16	-0.114 24	0.167 40	0.984 03	0.739 85

in two unknowns ( $b/a$  and  $b - a$ ) are established. When the equations are solved simultaneously,  $b/a$  and  $b - a$  are found.  $b$  and  $a$  can then be determined. Two polynomials were determined. The first, a quadratic, is appropriate for  $b/a \leq 14.55$ ; the second, a cubic, is necessary for  $14.55 \leq b/a \leq 63$ . The cubic will work for smaller ratios of  $b/a$ , but the quadratic is easier to evaluate.

For  $b/a \leq 14.55$ , values of  $A_0$ ,  $A_1$ , and  $A_2$  found for each  $\delta_1$  and  $\delta_2$  are substituted into eq 30.

$$\log\left[\frac{b}{a}\right] = A_0 + A_1 \log\left[\frac{5.9193(b-a)}{\delta}\right] + A_2 \left\{ \log\left[\frac{5.9193(b-a)}{\delta}\right] \right\}^2 \quad (30)$$

The values of  $A_0$ ,  $A_1$ , and  $A_2$  are listed in Table 4. The appropriate coefficients and  $\delta$  value are substituted into eq 30 to yield two equations in two unknowns. By equating the two equations to eliminate  $b/a$ ,  $b - a$  can be found first. Equation 30 can be used to find  $a$  and  $b$  with a relative error  $\leq 2.5\%$ , for  $b/a \leq 14.55$ .

For  $b/a \leq 63$ , the values of  $B_0$ ,  $B_1$ ,  $B_2$ , and  $B_3$  appropriate to each  $\delta_1$  and  $\delta_2$  are used to generate two equations in two unknowns by substituting into eq 31.

$$\log\left[\frac{b}{a}\right] = B_0 + B_1 \log\left[\frac{5.9193(b-a)}{\delta}\right] + B_2 \left\{ \log\left[\frac{5.9193(b-a)}{\delta}\right] \right\}^2 + B_3 \left\{ \log\left[\frac{5.9193(b-a)}{\delta}\right] \right\}^3 \quad (31)$$

$B_0$ ,  $B_1$ ,  $B_2$ , and  $B_3$ , are tabulated in Table 5. Eq 31 has three real roots, but it is easy to distinguish which is the correct answer. The equations can be solved by successive approximation. Alternatively, the working curve method can be used to arrive at a first approximation to  $b/a$  and  $b - a$ , and then the values can be further refined by fitting the two cubic equations. This method has a relative error of  $\leq 0.5\%$ .

**Table 6. Results of Applying the Proposed Methods to Experimental Data:**

system	parameter	SEM and CV data	method 1 <sup>a</sup>	method 2 <sup>b</sup>
$K_3Fe(CN)_6$ in $Na_2SO_4$	$a$ ( $\mu m$ )	3.5		3.2
	$b$ ( $\mu m$ )	20.1	21.0	18.4
	$b/a$	5.75	5.59	5.75
	$i_{ss}$ (nA)	1.85		
dopamine in HCl	$a$ ( $\mu m$ )	4.0		4.4
	$b$ ( $\mu m$ )	15.0	15.0	16.0
	$b/a$	3.62	3.62	3.64
	$i_{ss}$ (nA)	4.50		

<sup>a</sup> Value of  $a$  found by SEM is used in eq 29 to determine  $b$ . <sup>b</sup>  $a$  and  $b$ , determined by eq 31, are compared to SEM values.

To summarize,  $a$  and  $b$  can be determined as follows.

1. If the shield is of infinite thickness and steady state can be reached,  $a$  can be found using eq 27. ( $\Delta E_{1/2}$  must approach 0 V, which is unlikely for an electrode larger than about  $1 \mu m$ .<sup>26,27</sup>)

2. If  $a$  is already known, and  $b$  is known to be less than  $l$  at steady state ( $\Delta E_{1/2} = 0$ ),  $b$  can be calculated using eq 29 or extracted from Figure 5.

3. If  $a$  and  $b$  are both unknown, several steps are needed to find both values. First, take a cyclic voltammogram at a sufficiently slow sweep rate to achieve steady state ( $\Delta E_{1/2} = 0$ ). Proceed, as outlined above, to find ratios of  $i_p/i_{ss}$  at two scan rates that are sufficiently rapid to generate cyclic voltammograms with peak currents. Then,  $a$  and  $b$  are found by using either the working curves in Figure 8 or the appropriate polynomial equation (eq 30 or 31), depending on the accuracy needed and whether  $b/a$  is less than or greater than 14.55.

**Experimental Evaluation of the Method.** Potassium ferricyanide (2.0 mM) with sodium sulfate (0.1 M) and dopamine (2.0 mM) with HCl (0.1 M) were used as test solutions to evaluate the simulation results. Ferricyanide is reduced by one electron and dopamine is oxidized by two electrons. Both reactions are reversible at the scan rates employed. The diffusion coefficients of the redox couples are  $6.5 \times 10^{-6}$  and  $6.4 \times 10^{-6} \text{ cm}^2/\text{s}$ , respectively.<sup>32,33</sup> Different finite glass-shielded microelectrodes were used for each system. The disk and shield radii were determined by scanning electron microscopy as reported in Table 6. Both steady state and nonsteady state cyclic voltammograms were recorded. The experimental steady state currents are cited in Table 6. The data were analyzed to test two methods. First, the values found for  $a$  by SEM were used to test the results parameterized by eq 29. This is called method 1 in Table 6.  $i_{disk, semi-\infty}^{ss}$  was calculated from  $a$ .  $Z_{ss}$  was then calculated, and  $a/b$  extracted from Figure 5 and eq 29. The values found for  $b$  in each case agree within 5% with the values found by SEM. Second, values for both  $a$  and  $b$  were determined from Figure 8 and eq 31 without using the SEM information. This is called method 2 in Table 6. In both cases, the values for  $a$  agreed within 10% with the values found by SEM, and  $b$  agreed within 7–8%. The methods developed from the simulation predict agreement within 0.5%. Closer examination of the SEMs revealed the disk and

(32) Adams, R. N. *Electrochemistry at Solid Electrodes*; Marcel Dekker: New York, 1969; pp 219–222.

(33) Nagy, G.; Gerhardt, G.; Okee, A. F.; Rice, M. E.; Adams, R. N.; Moore, R. B., III; Szentirmay, M. N.; Martin, C. R. *J. Electroanal. Chem.* **1985**, *188*, 85–94.

insulator were not perfectly flush. The accuracy of the experimental determination probably suffered because of electrode construction and the limitations of measuring the peak and steady state currents. Within these limitations, the simulation is consistent with the experimental results.

## SUMMARY

1. A two-dimensional, nonuniform EESG has been successfully employed in the simulation of the cyclic voltammetric response of inlaid disks with shields of thickness comparable the electrode radius. The nonuniform EESG yields better precision and accuracy in the simulation of the voltammetric responses of inlaid microdisk electrodes than a uniform EESG. The improvement arises from a more accurate simulation of the concentration profiles at the interfaces of the disk and insulator, and insulator and solution.

2. As the ratio of the disk and insulator radius ( $b$ ) to disk radius ( $a$ ) increases, steady state current ( $i_{ss}$ ) increases. When  $b \rightarrow a$ ,  $i_{ss}$  is 49% higher than the current for a disk of the same size embedded in an infinite insulator. The relationship between  $i_{ss}$  and  $b/a$  has been found and verified experimentally.

3. For inlaid disks with shields of finite length, diffusion from behind the plane of the electrode not only enhances  $i_{ss}$  but also enhances the rate at which steady state ( $\Delta E_{1/2} = 0$ ) is achieved

as compared to an inlaid disk with an infinitely thick insulator. At steady state, flux from behind the plane of the electrode brings the diffusion field close to a spherical geometry. At steady state, whether  $b$  is infinite or finite, the ratio of the current to the steady state current is governed solely by the Nernst equation.

4. Two different ways to determine  $a$  and  $b$  from simple experimental results are provided. The theoretical accuracy is within 0.5%, while application to experimental results was accurate to within 10%. Electrode construction and the precision of determining the current are probably important limitations in the application of this method.

## ACKNOWLEDGMENT

We thank Stephen W. Feldberg of Brookhaven National Laboratory for helpful discussion, and we acknowledge the Research Foundation of the City University of New York for a PSC Award (668269) and the National Science Foundation for a grant (CHE-88-15936/92-96013).

Received for review July 5, 1994. Accepted December 8, 1994.<sup>®</sup>

AC940671D

---

<sup>®</sup> Abstract published in *Advance ACS Abstracts*, January 15, 1995.